In-Situ Cross-linking of Silane Functionalized Reduced-Graphene Oxide and Low-density Polyethylene

Syeda S. Abbas[1], Gregory J. Rees[2], Georgios Patias[3], Claire E.J. Dancer[1], John V. Hanna[2] and Tony McNally[1]*

[1]International Institute for Nanocomposite Manufacturing (IINM), WMG, University of Warwick, CV4 7AL, UK

Departments of [2]Physics and [3]Chemistry, University of Warwick, CV4 7AL, UK

*Corresponding Author. Email: t.mcnally@warwick.ac.uk (Tony McNally)

Telephone: 0044 (0)24 7657 3256

Abstract

Vinyl trimethoxysilane (VTMOS) functionalized reduced graphene oxide (rGO) was melt blended with low-density polyethylene (LDPE) and cross-linked through the vinyl group using a free radical initiator, dicumyl peroxide (DCP), in an extruder. The cross-linking reaction of the pendant vinyl group on the silane with LDPE via peroxide initiation was confirmed by, solid-state magic angle spinning (MAS) ^{13}C and ^{29}Si nuclear magnetic resonance (NMR) measurements. The Raman spectrum of the crosslinked VTMOS-rGO and LDPE confirmed the formation of a 3D network. Scanning electron (SEM) and transmission electron (TEM) microscopy with elemental mapping showed the VTMOS forms nano-spheres located interstitially between rGO layers dispersed within the LDPE matrix. From oscillatory rheology measurements the transition to more 'solid-like' behaviour due to crosslinking was detected from a significant decrease in the crossover frequency (G′v G″) from 31.6 (rad/s) to as low as 0.603 (rad/s) and increase in

relaxation times (λ) from 0.032s to 1.66s for a rGO loading of 1wt%. The formation of a 3D interconnected cross-linked VTMOS-rGO-LDPE network resulted in an increase in the tensile strength (↑31%) and tensile stress at break (↑55%) of LDPE. The onset of thermal degradation of LDPE was delayed by up to 31 °C due to the formation of cross-links and inclusion of silane functionalised rGO which requires a higher activation energy to initiate degradation.

Keywords: reduced graphene oxide (rGO), vinyltrimethoxysilane (VTMOS), silane nanospheres, low density polyethylene (LDPE), composites

1. Introduction

Considerable attention continues to be focused towards graphene (and the graphene family of materials) due to its high surface area (>2600 m^2 g^{-1})[1], exceptional thermal conductivity (~3000 W m^{-1} K^{-1})[2], mechanical properties (Young's modulus of up to 1 TPa)[3-5], electrical conductivity (2 x 10^3 S cm^{-1})[6] and 97.7 % optical transparency[7-8]**.** A single graphene sheet consists of a monolayer of sp^2 hybridised carbon atoms in a two dimensional lattice, densely packed in a honeycomb structure of individual layers. Even though, this material has strength comparable to diamond, it is still flexible enough to be wrapped into 0-D fullerenes, rolled into 1-D nanotubes or even stacked into 3-D graphite[9]. Due to its extraordinary set of properties, it has potential for uses ranging from catalysis**,** in energy storage devices[10], for biomedical purposes like in cancer therapy[11] as well as for drug delivery[12] and can also be incorporated into polymer matrices to produce functional composite materials[13]. However, with regard the latter there are significant

technical challenges in translating these exceptional properties from graphene materials to a polymer matrix.

Key to achieving this is the effective uniform dispersion and distribution of the graphene material (nanofiller) throughout the polymer matrix combined with enhanced interfacial-interaction between the blend components[14]. In achieving both, any load or stress applied to the polymer matrix, would be transferred to the nanofiller which is highly dependent on the polymer-nanofiller interface[15] and the, size and properties of the interphase region. Due to the lack of functional groups on the surface of graphene(s) and its high specific surface area, it tends to agglomerate within the polymer matrix due to strong van der Waals interactions and π-π bonding between graphene layers making them insoluble in polymers [16-17]. Therefore, to minimise agglomeration, graphene needs to be modified with functional groups that are compatible with or encourage interfacial interactions with the polymer of interest [18-19]. Unlike single sheet pure graphene, graphene oxide (GO) has various functional groups such as carbonyls and other polar moieties present on the basal planes and at sheet edges which help to homogenously disperse GO in water and other polar solvents. The presence of different functional groups provide reaction sites for further functionalisation and reaction with polymers.

Organosilanes have recently been used to promote interfacial interactions between nanofillers and different polymers. These silane agents consist of $(R_1, R_2, R_3)SiX_n$, where X is usually a hydrolysable group to form $RSi(OH)_3$, whereas the R group usually remains unreactive [20]. Silanization of GO has been investigated, with silane agents such as aminopropyltriethoxysilane (APTES)[21-26], triethoxymethoxysilane (MTES), 3-glycidyloxypropyl trimethoxysilane (GPTMS) [27-29] and trimethoxysilane (TEOS)[30-32].

Due to their polar groups they provide compatibility with non-polar polymers and are widely used as coupling agents for cross-linking of poly(olefin)s and other polymers.

Vinyl alkoxy silanes such as vinyltrimethoxy silane (VTMOS) have also been explored and is the most common silane used for cross-linking polyethylene (PE) due to the pendant vinyl bond that allows it to rapidly cross-link. Silane grafting entails cross-linking of the vinyl group onto the PE chain *via* a free radical reaction. A second stage includes exposure of the copolymer to hot water or steam for hydrolysis of the alkoxy groups on the silane to form stable siloxane linkages. This silane cross-linking method has many advantages over other cross-linking methods, such as ease of processing and is currently being successfully exploited on a large commercial scale to produce cross-linked polyethylene for application in electrical cable insulation and pipes [33].

Recently Wang *et al*. functionalised GO using vinyltriethoxy silane (VTES) under acidic conditions followed by a reduction reaction using basic conditions to synthesise VTES-rGO [25]. This was then blended with a LDPE matrix *via* solvent mixing and the mechanical and barrier properties of the composites measured. Silane functionalisation resulted in an increase in mechanical properties however, this method is limited in scalability due to the use of organic solvent and limited dispersion of the VTES-rGO. Although this technique is most effective at forming composites with low graphene content, it is not practical because these polymers (e.g. poly(ethylene)) only dissolve in certain solvents such as xylene, toluene or trichlorobenzene above 120°C and therefore this approach has limited applicability and scalability.

In contrast, melt mixing using twin screw extruders allows for the production of such composites in large quantities. By varying extruder temperature, screw profile and

screw speed, effective dispersion and distribution of nanofillers within polymer matrices can be achieved [34]. Recently Lin *et al*. studied the effects of melt blending graphene nanoplatelets (GNPs) relative to GO as reinforcing fillers for high-density polyethylene (HDPE) and used VTMOS to provide adhesion between the GNP and HDPE. With inclusion of the silane compatibiliser a 56% increase in elastic modulus and 23% increase in maximum stress for a relatively high 10wt% GNP loading was achieved. However, GNP agglomerations were also observed in the HDPE matrix by SEM [35].

In our previous work, GO was successfully functionalised and thermally reduced to achieve vinyltrimethoxysilane reduced graphene oxide (VTMOS-rGO) nano-spheres that were located in the interlayer spacing between rGO sheets. This was achieved *via* an acid-base reaction using aqueous media to form silane networks with free vinyl groups available for further reaction. The mechanism of silanization of rGO and the formation of a silane network was confirmed from rigorous characterization using a range of techniques [36]. Critically, the availability of free vinyl pendant groups in the silane network provides a route to cross-linking GO with polymer matrices.

In this work, we report the preparation *via* melt blending and the characterisation of LDPE crosslinked with rGO functionalised with VTMOS to make VTMOS-rGO-LDPE (or m-G-LDPE as referred to in the paper). The unreacted vinyl pendant group reacts with the LDPE chains *via* a free radical initiated reaction during melt blending in an extruder, resulting in a 3D network composed of LDPE and VTMOS-rGO.

2. Materials and Methods

2.1 Synthesis of VTMOS-rGO

GO purchased from Abalonyx, VTMOS (98%) purchased from Alfa Aesar, Hydrazine Hydrate (78-82%) and Ammonia solution (2M in methanol) purchased from Honeywell Fluka, Hydrochloric acid (37%) from Fisher Chemical. LDPE (material grade LD 605BA, melt flow rate (MFR) = 6.5 g/10 min as reported in data sheet provided by the supplier), purchased from ExxonMobil, Baytown, TX, USA, and delivered in pellet form. DCP (98%) (density 1.56 g/ml at 25°C) purchased from Sigma Aldrich. To modify GO, a dilute mixture of HCl (0.40M) and VTMOS was added to GO and heated for 2 hours at 70 °C in water yielding a dark brown solution formed by stirring and heating. After the allocated time, a hydrazine/ammonia mixture was added and heated for another 4 hours at 90°C under reflux. After stirring, this mixture was filtered and washed with water until the pH became neutral (pH=7) and then dried in a vacuum oven. For further details see our previous publication [36].

2.2 Composite Preparation

LDPE pellets were firstly cryo-milled to form a powder, using a SPEX® SamplePrep Freezer Mill (Stanmore, UK). LDPE pellets were cooled for 10 minutes using liquid nitrogen followed by 2 x10 min grinding cycles at 15 Hz. After each cycle, the sample was cooled for a 5 minute interval. After cryo-milling, the LDPE powder was dried in a vacuum overnight at 40 °C for 12h prior to processing. Composites were prepared by blending a given amount of VTMOS-rGO in LDPE to achieve the following GO loadings; 0.1wt%, 0.5wt%, 1.0wt%, 3.0wt% and 5.0wt%. The initiator, dicumyl peroxide (DCP) was also dry-blended with each blend formulation at a loading equivalent to 0.1wt% LDPE. This pre-blend was then added to a ThermoFisher Scientific PRISM co-rotating 16mm Eurolab twin screw extruder and processed in the temperature range 140-150°C at 50 rpm. Extruded pellets were then injection moulded using a piston

injection moulding system (Thermo-Scientific Haake™ MiniJet Pro) to prepare standard dumbbell-shaped specimens according to ASTM D68 V for tensile testing and disk shaped samples (d=25, h=1.5 mm) for oscillatory rheology and XRD measurements. The injection temperature was set to 150°C, the mould temperature to 60°C and an injection pressure of 200 bar employed. A set of control samples were also prepared by melt mixing using the same processing conditions, i.e. blends of rGO and LDPE where the rGO has not been modified with VTMOS.

2.3 Characterisation

Solid state ^{13}C magic angle spinning (MAS) nuclear magnetic resonance (NMR) measurements were undertaken at 7.05 T ($\nu_0(^1H)$ = 300 MHz, $\nu_0(^{13}C)$ = 75.8 MHz) using a Bruker Avance HD-300 MHz spectrometer. A Bruker 4 mm HX MAS probe was utilised to enable a MAS frequency (ν_r) of 12 kHz. These measurements were undertaken using single pulse (direct detection) experiments using a $\pi/2$ ^{13}C excitation pulse of 4μs, a recycle delay of 60s, and a ^1H decoupling field strength of 100 kHz during data acquisition. All ^{13}C data were indirectly referenced to neat TMS (δ 0 ppm) *via* a secondary solid alanine reference that provides three distinct resonances for the methyl, backbone and carbonyl carbons at chemical shifts of δ 20.5, 50.5 and 178ppm, respectively. Variable temperature ^{13}C MAS NMR measurements acquired over a 298.1 - 415.1 K range were undertaken using a 7 mm Bruker HX probe utilising ceramic rotors and rotor caps. The temperature was ramped and stabilised over a period of 10 minutes, before each experiment was acquired. These measurements were also undertaken using single pulse (direct detection) experiments using a ^{13}C excitation pulse of 4μs, a recycle delay of 60s, and a ^1H decoupling field strength of 100 kHz during data acquisition. Accompanying ^{29}Si MAS NMR data were recorded at 7.05 T ($\nu_0(^{29}Si)$ = 59.6 MHz, $\nu_0(^1H)$ = 300.1 MHz)

using a Bruker Avance HD 300 MHz spectrometer. A Bruker 7 mm HX MAS probe was utilised to yield spinning frequencies (ν_r) of 5 kHz. Single pulse (direct detection) experiments were again utilised; these consisted of a $\pi/2$ ^{29}Si excitation pulse of 6.0 μs pulse, a recycle delay of 10 s (verified by measurement), and a ^{1}H decoupling field strength of 80 kHz during data acquisition. The ^{29}Si pulse length was calibrated using solid kaolinite which also acted as an external chemical shift reference (δ −93 ppm w.r.t. TMS, δ 0 ppm).

Raman spectra were recorded on a Renishaw inVia Reflex Raman microscope with a 532nm excitation source and a 100x microscope objective. The samples examined were in disc form.

For tensile testing, a Shimadzu Autograph AGS-X frame was used and equipped with a 10kN load cell with a twin TRViewX non-contact digital video extensometer (500mm and 120 mm field of view). Data was captured using Trapezium X Version 1.4 package software and the samples tested were standard dumbbell-shaped test specimens (ASTM D638 V) with an extensometer gauge length of 7.62mm. Testing was performed using a constant crosshead speed of 10 mm/min. 10 replicates of each composite were tested to obtain an average and standard deviation values.

Dynamic mechanical thermal analysis (DMTA) measurements were carried out using a Triton Tritec 2000 DMA equipped with a standard air oven. The samples studied were taken from injection moulded bars and cut to the required length (50 mm). Measurements were performed in a dual cantilever mode with a free length of 17.50mm, width of 10 mm and thickness of 4 mm.

A Thermo Scientific Haake MARS III rheometer with parallel-plate geometry was used to study the rheological behaviour of the composites and the extent of GO dispersion in the LDPE matrix. The samples first underwent oscillatory amplitude stress sweeps over a stress range of 0.1-100 Pa at a fixed temperature and frequency of 160°C and 1Hz, respectively. After determining the stress at which the storage modulus is independent of deformation, frequency scans were performed from 0.1-100 Hz under a controlled stress of 10 Pa in an air atmosphere.

Scanning electron microscopy (SEM) images were obtained using a Zeiss sigma field emission instrument. For sample preparation, the samples were cryo-fractured by placing them in a bath of liquid nitrogen for 30 minutes and then striking them. The fractured surfaces were attached on aluminium SEM stubs using carbon adhesive tape with the fractured surface facing upwards. The samples were also sputter coated (10nm) by an Au/Pt metal target (Cressington 108 auto) to minimise charging effects

Composite samples for transmission electron microscopy (TEM), were ultra-cryomicrotomed with a diamond knife at -130°C into 200nm thick slices using a Lycia RM2245 ultra-cryomicrotome equipped with a Diatome and the samples were then placed onto holey carbon grids. The samples were examined using a Jeol 2100 TEM fitted with a Gatan Ultrascan 1000 camera. TEM/STEM micrographs were obtained using a Talos (FEI) F200X with Super-X EDS operated at 200kV for both TEM and STEM elemental mapping.

X-ray Diffraction measurements were completed on a Panalytical Empyrean instrument in Bragg–Brentano geometry with Co-K_α radiation (1.7903 Å) and a solid-state Pixcel detector for fast data collection. A variable divergence slit was used to control the size of

the beam on the sample to be 6mm parallel to the beam and a beam mask of 15mm. 20 minute scans were collected in the range 4–40° 2θ with a step size of ~0.026° 2θ.

Differential Scanning Calorimetry was performed on a Mettler Toledo (DSC1, model 700, 400W) and the data collected evaluated using a STARe Version 15.01 software package. The samples were studied in the range 25°C to 200°C using a heating and cooling rate of 10 K/min for two cycles.

Thermogravimetric analysis was carried out using a Mettler Toledo thermal analyzer over the temperature range of 25 °C to 800 °C at a heating rate of 10°K min^{-1} under nitrogen.

3 Results and Discussion

Cross-linking of LDPE occurs at elevated temperatures, initiated by DCP, which first decomposes and then forms oxy radicals. These radicals extract hydrogen from the LDPE chains and/or from the vinyl group of the silane modified rGO and therefore produce a free radical PE or silane, as illustrated in Scheme 1. These free radicals then attack other molecules in the same way, initiating a free-radical reaction for formation of covalent attachment of the silane modified rGO to the LDPE chains, resulting in a cross-linked system, see Step 5 of Scheme 1 [37].

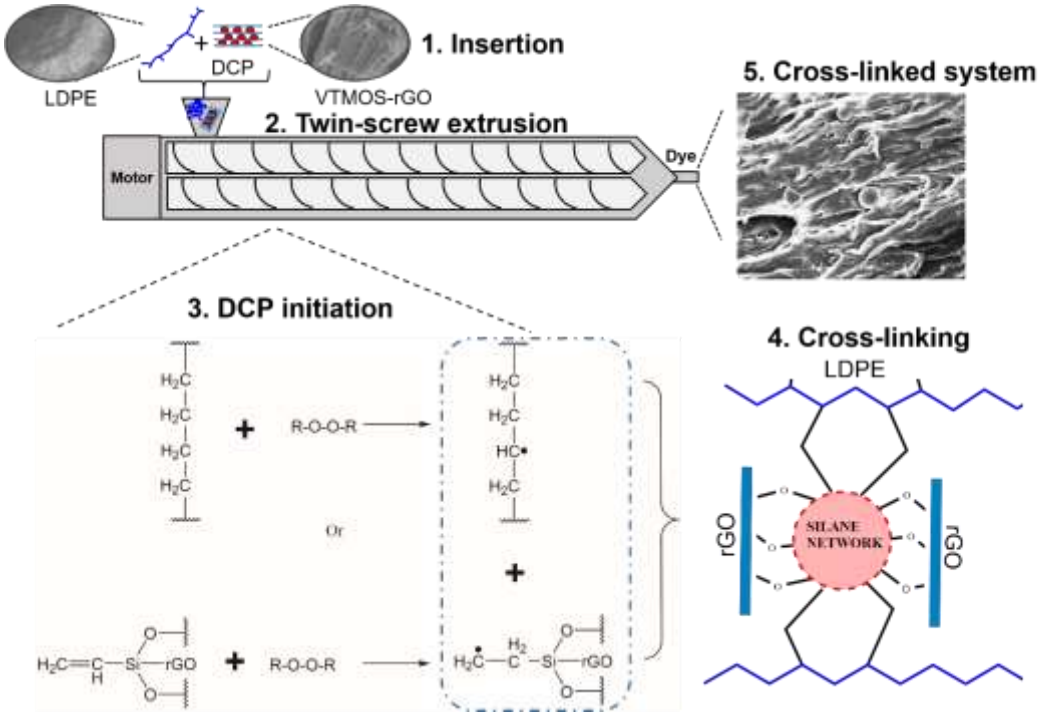

Scheme 1. Schematic illustration of the steps in the preparation of m-G-LDPE. Step 1: Insertion of VTMOS-rGO(powder), LDPE (powder) and DCP into the hopper. Step 2: Melt mixing of components. Step 3: DCP initiation during extrusion, two routes, either through LDPE or silane radicals. Step 4: Cross-linking of both systems. Step 5: VTMOS-rGO-LDPE network structure formed (SEM image shows silane spheres within the LDPE matrix).

Prior to the addition of VTMOS-rGO to LDPE, the ^{13}C MAS NMR spectrum of LDPE consists of a single major resonance at 28 ppm corresponding to the main chain methylene species. Additional resonances are present at 12 and 13 ppm, which are attributed to the methyl and methyne functional groups, respectively (see Figure 1a)) [38]. After functionalisation, the major resonance at 28 ppm becomes multi-component thus splitting into three resonances with chemical shifts at 26, 29 and 31 ppm (see Figure 1b)). The additional resonance at 26 ppm corresponds to the methyl attachment from the vinyl to the LDPE chain [39]. The further splitting of the 28 ppm main resonance into two

resonances (29 and 31 ppm) is attributed to the cross-linking of small polymer branches to the main longer branches, confirmation that some of the LDPE chains have cross-linked to themselves. An *in-situ* ^{13}C MAS NMR experiment was undertaken to replicate the grafting of LDPE to the functionalized GO, where the VTMOS-rGO was added to LDPE and DCP inside a 7mm Bruker MAS (5 kHz) rotor with a zirconia cap containing a vent. The temperature was ramped from 298.1 K to 415.1 K to replicate the temperature profile in the extruder and a heat to experiment increment of 10 K per ^{13}C MAS NMR experiment completed. This variable temperature study was performed to observe the reaction temperature required to graft LDPE and the modified GO. At approximately 358.1 K, a resonance at 26 ppm begins to evolve and become prominent, corresponding to the vinyl reaction with the LDPE chains *via* a radical initiation step. At the same temperature, the resonance at 31 ppm starts to form and, this is attributed to the intermediate length chains of the LDPE cross-linking with the main long LDPE chains. This *in-situ* ^{13}C MAS NMR study (MAS frequency ν_r = 5 kHz) shows that both, the cross-linking of LDPE with itself and the vinyl attachment of the silane grafted GO attached to the LDPE chain, takes place at a similar temperature of ~370 K. This assertion was confirmed by a ^{29}Si MAS NMR study (MAS frequency ν_r = 5 kHz) of VTMOS-rGO before and after addition to the LDPE matrix (see Figure 1d) and 1e)). Before addition to LDPE, VTMOS-rGO shows three broad ^{29}Si resonances assigned to T_1, T_2 and T_3 silicon environments, as shown in Figure 1d). The T_1 and T_2 resonances are exclusively the product of monomers and dimers, whilst the T_3 resonance represents the trimeric and larger structures pertaining to the VTMOS polymer grafted to the rGO. After addition of the modified GO to the LDPE matrix, a detectable increased proportion in the T_1 component is observed (see Figure 1e)) in comparison to the original T_1:T_2:T_3 ratio of the

ungrafted sample shown in Figure 1d), thus suggesting that the silane is bonded to the GO and the polymer and, there is only a single attachment of the siloxane bond. The increase in the proportion of T_1 from Figure 1d) to Figure 1e), suggests that before addition of the polymer there is a substantial silane network bonded to the rGO, and after addition to the LDPE matrix, a proportion of the silane becomes attached to the LDPE matrix. As shown in Figure 1e), the presence of T_2 and T_3 in the grafted sample demonstrates that a siloxane network is still present; however, the increase in the T_1 component shows that more of the silane is now bonded to the polymer. These multinuclear ^{13}C and ^{29}Si MAS NMR studies confirm the covalent attachment via the silane vinyl on the modified rGO to the LDPE chains.

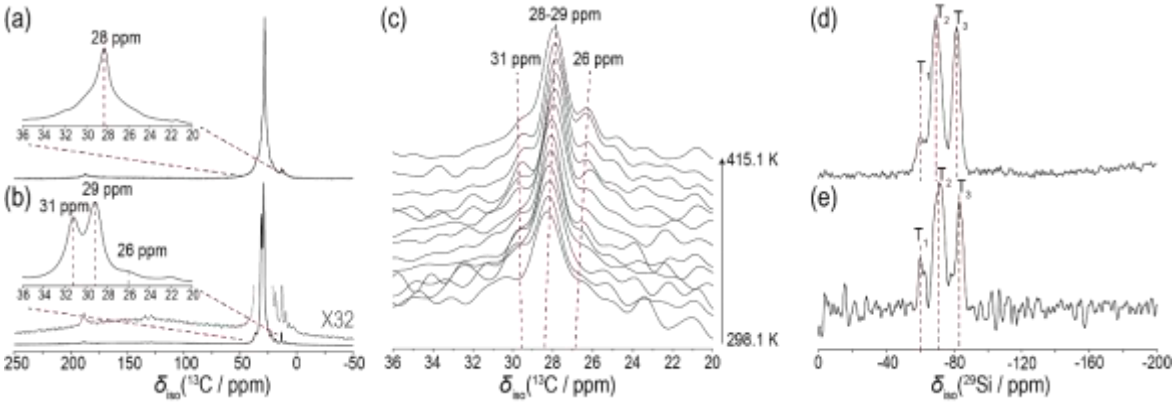

Figure 1. a) ^{13}C MAS (12 kHz) NMR of LDPE, insert shows an expansion of the region between 36-20 ppm. b) ^{13}C MAS (12 kHz) NMR of m-g-LDPE, insert shows an expansion of the region between 36-20 ppm. A x32 expansion of the baseline shows the vinyl resonances and the sp^2 graphene resonance is given in grey. c) The *in-situ* grafting of LDPE to the functionalised GO, between 298.1 K and 415.1 K (increments of 10 K) d) ^{29}Si MAS (5 kHz) NMR of functionalised GO and e) ^{29}Si MAS (5 kHz) NMR of m-g-LDPE.

Confirmation of the formation of the m-g-LDPE network was also obtained by Raman spectroscopy. The main characteristic peaks in the Raman spectrum of LDPE are C-C stretching at 1063cm^{-1} and 1126cm^{-1}, C-C twisting at 1295cm^{-1} and bending of CH_2 at 1441cm^{-1} [40]. These peaks were also present for both rGO filled LDPE and m-G-LDPE, as well as additional peaks observed for the GO defect structures, D peak (~1347 cm^{-1}), and the in-phase vibration of sp^2 carbon atoms, G peak (~1590 cm^{-1}), see Figure 2. The ratio of the intensity of the D to G peaks (I_D/I_G) describes the number of defects within the composite material. For the m-G-LDPE composites, I_D/I_G = 1.40 whereas the I_D/I_G for rGO-LDPE = 1.34 and is due to functionalisation of the modified graphene with the polymer relative to the unmodified rGO based composites. The up-shifting of the D and G bands shows the strong compressive forces the polymer exerts on the m-G-LDPE and the load transfer that proved successful between the filler and polymer matrix [41].

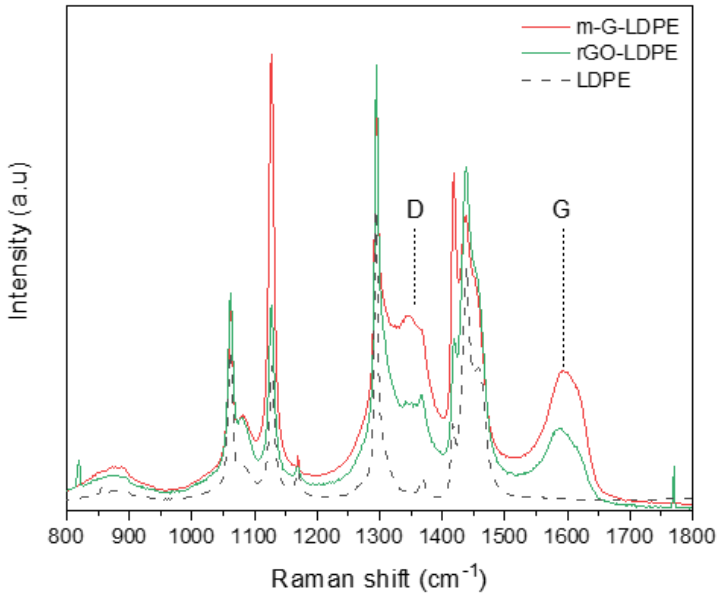

Figure 2. Raman shift of unfilled LDPE, m-G-LDPE and rGO-LDPE for a rGO loading of 5wt%.

To study the effect of crosslinking on the morphology of the composites all samples were examined using both SEM and HRTEM using a number of different modes. SEM images were taken from cryo-fractured surfaces of the composites, see Figure 3. For the neat LPDE the fractured surface was smooth relative to that seen for the neat LDPE cross-linked with 0.1wt% DCP, where failure shows the formation of a fibre-like structure. This is a direct result of the crosslinking of LDPE by DCP, the fibrillar structure formed by the orientation and alignment of micro-fibrils as a result of the longitudinal sliding motion and the destruction of the PE lamellae structure [42]. This fibrillar morphology was also observed for the composites. After functionalisation the modified rGO was uniformly dispersed within the matrix. Combined, uniform dispersion of modified rGO in the LDPE matrix and the formation of a fibrillar morphology are known to enhance mechanical properties of polymers [43-44]. At higher loadings the modified rGO e.g. 5wt%, a network of siloxane spheres can be observed within the fibrillar polymer structure, verified by EDS measurements, see inset in Figure 3.

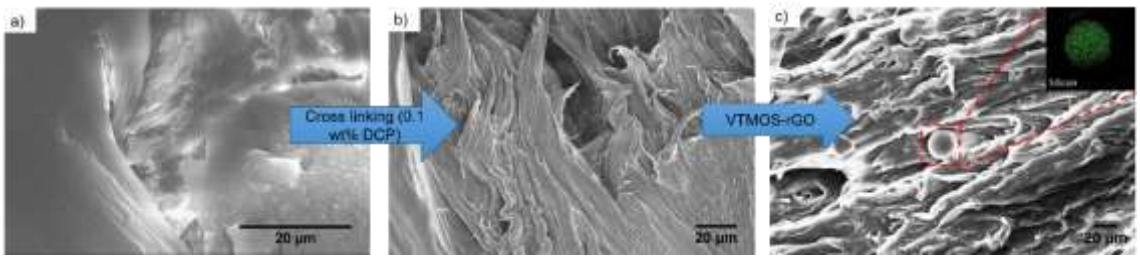

Figure 3. SEM micrographs of a) neat LDPE, b) LDPE cross-linked with DCP and c) VTMOS-rGO (5wt%) modified LDPE cross-linked with DCP (m-G-LDPE).

The morphology of the composites was also examined by HRTEM, see Figure 4. The TEM image of VTMOS-rGO before extrusion shows a uniform distribution of silane nanospheres on the surfaces of the rGO layers. As expected, the neat LDPE shows no characteristic features. Post extrusion, the silane spheres are within the graphene layers

which in turn are dispersed within the LDPE matrix. These images confirm layers of rGO present within the LDPE matrix, with silane based spheres located between the layers.

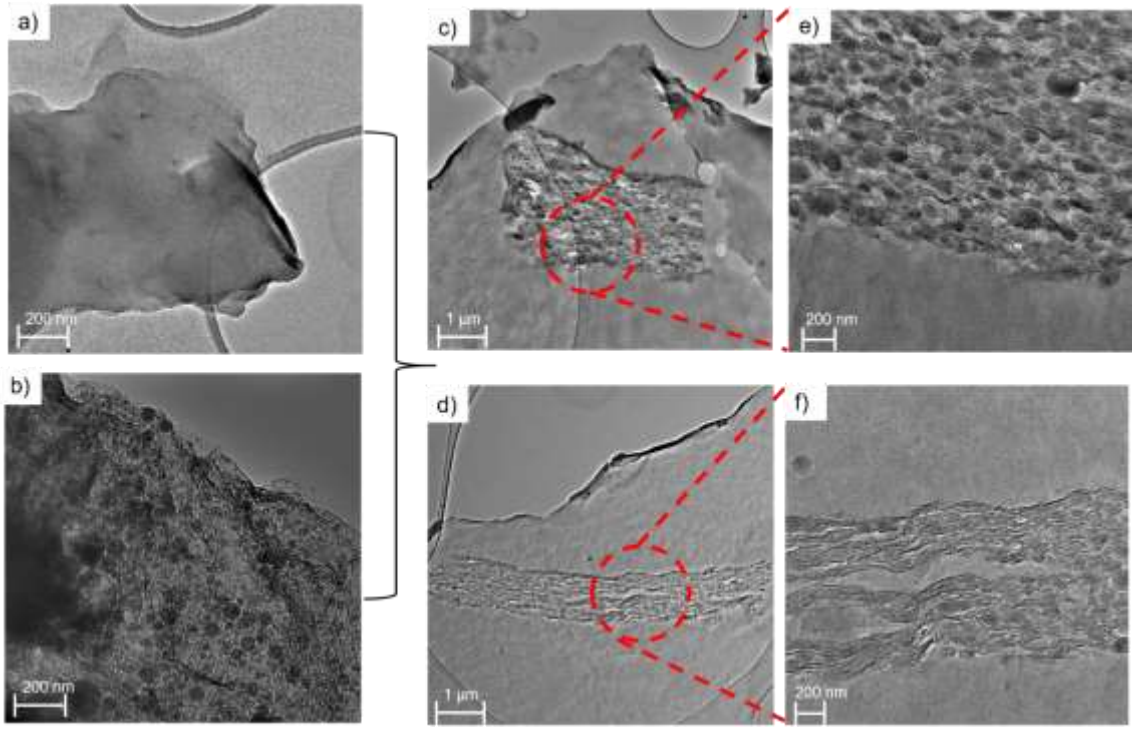

Figure 4. TEM images of neat a) LPDE, b) VTMOS-rGO and composites produced after extrusion of both, c)-f)VTMOS-rGO-LDPE. e)-f) zoomed in versions of c)-d).

To further verify this morphology TEM bright field (BF) and high-angle annular dark-field (HAADF) images were obtained and, elemental mapping (EDS) of the samples performed, see Figure 5. The darker region of the BF image shows clusters of silane spheres within layers of rGO and with HAADF imaging, the polymer can be seen behind the VTMOS-rGO. Through elemental mapping, the cluster of spheres observed can be verified as silane based nanospheres (green) within wrinkles and layers of rGO.

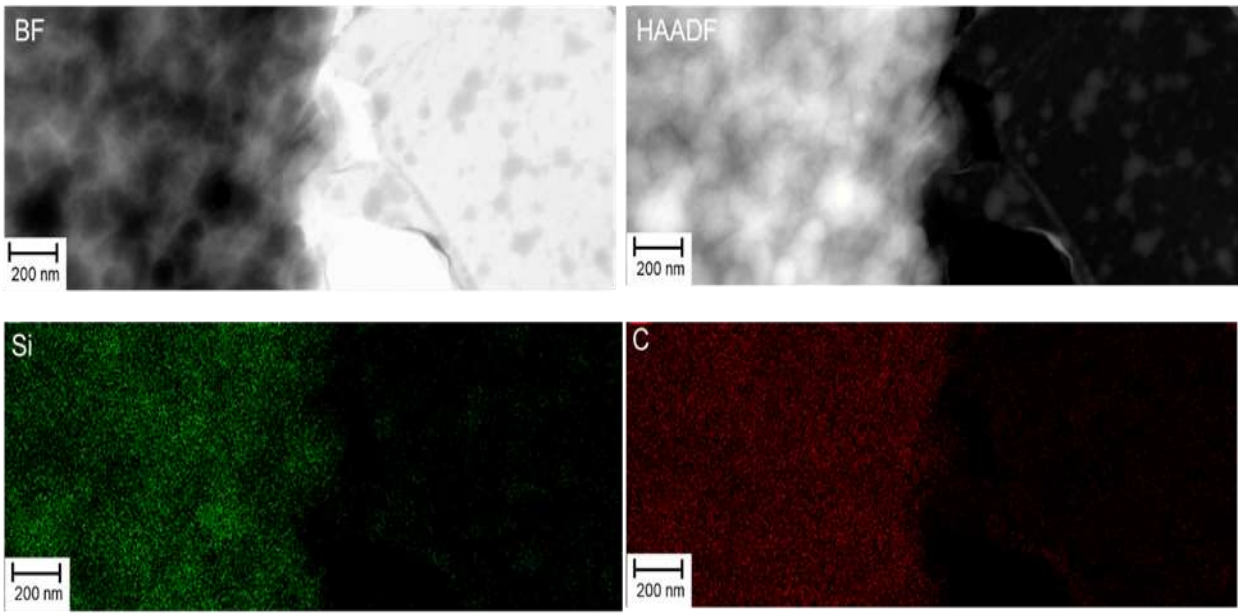

Figure 5. TEM-EDS BF and HAADF images of VTMOS-rGO-LDPE. Elemental mapping showing silicon (green) and carbon (red). Each map is independent of its own maximum intensity.

Specifically, with regard the composite materials, comparing the TEM images of rGO-LDPE with those of VTMOS-rGO-LDPE in the range 200nm to 500nm (see Figure 6), the silane modified rGO is well dispersed in the LDPE matrix. Furthermore, the silane nanospheres formed from the VTMOS modification of rGO are located between the rGO layers, helping to exfoliate them. Nanospheres can also be observed dispersed throughout the LDPE matrix, confirmed by both SEM and TEM imaging and further validated from TEM-EDS experiments. The observations made from EM microscopy imaging suggest strong interfacial interaction between the VTMOS treated rGO and LDPE, which should result in enhanced mechanical properties and alter the viscoelastic behaviour of LDPE.

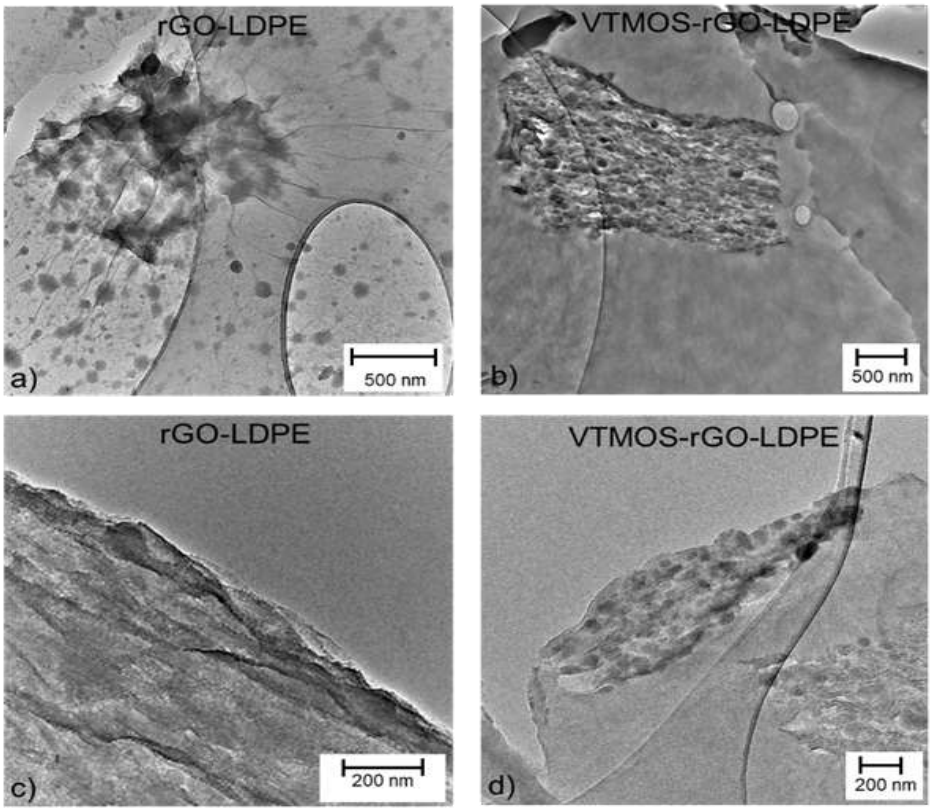

Figure 6. TEM images of a) and c) rGO-LDPE and b) and d) VTMOS-rGO-LDPE, (scale bars 500nm and 200 nm), respectively.

If a silane functionalized rGO-LDPE cross-linked network has formed, this should result in changes in the stiffness and strength of LDPE but a reduction in ductility. Figure 7 shows the Young's modulus (E), tensile strength (σ), elongation at break (ε) and tensile stress at break (σ_b) for neat LDPE with and without DCP, and for the composites of rGO-LDPE and m-G-LDPE. A decrease in E was observed for the m-G-LDPE composites (Figure 7a)) relative to the other composites which is due to the introduction of cross-links resulting in decreased LDPE crystallinity [45]. Furthermore, σ and σ_b are higher for m-G-LDPE relative to neat LDPE, and for the composites with rGO. σ for rGO-LDPE increased from 14.98 MPa to 16.40 MPa (↑~8.5%) on addition of 5wt%, whereas for the same loading the increase was to 19.68 MPa (↑~25%) for m-G-LDPE. Due to the vinyl

cross-linking of the silane grafted rGO to LDPE, load transfer across the interface was more efficient and the stress (tensile) was more uniformly distributed through unit volume of sample when the external force was applied, resulting in an increase in σ for the m-G-LDPE composite [45, 46].

However, as expected ε for the m-G-LDPE composites was the lowest overall, a 36% decrease for the composite with 5wt% VTMOS-rGO, whereas for the un-crosslinked rGO composites, ε was similar to the neat polymer. The decrease in ε is caused by the enhanced interaction of the silane modified GO with the LDPE *via* the crosslinks formed with LDPE during melt mixing. The mobility of the LDPE chains are more restricted causing a reduction in the ductility of the composites [46-47]. Similar behaviour has been reported for peroxide cross-linked poly(ethylene) alone, again associated with the restrained mobility of polymer chains which resist applied stress resulting in a decrease in ε[45, 48].

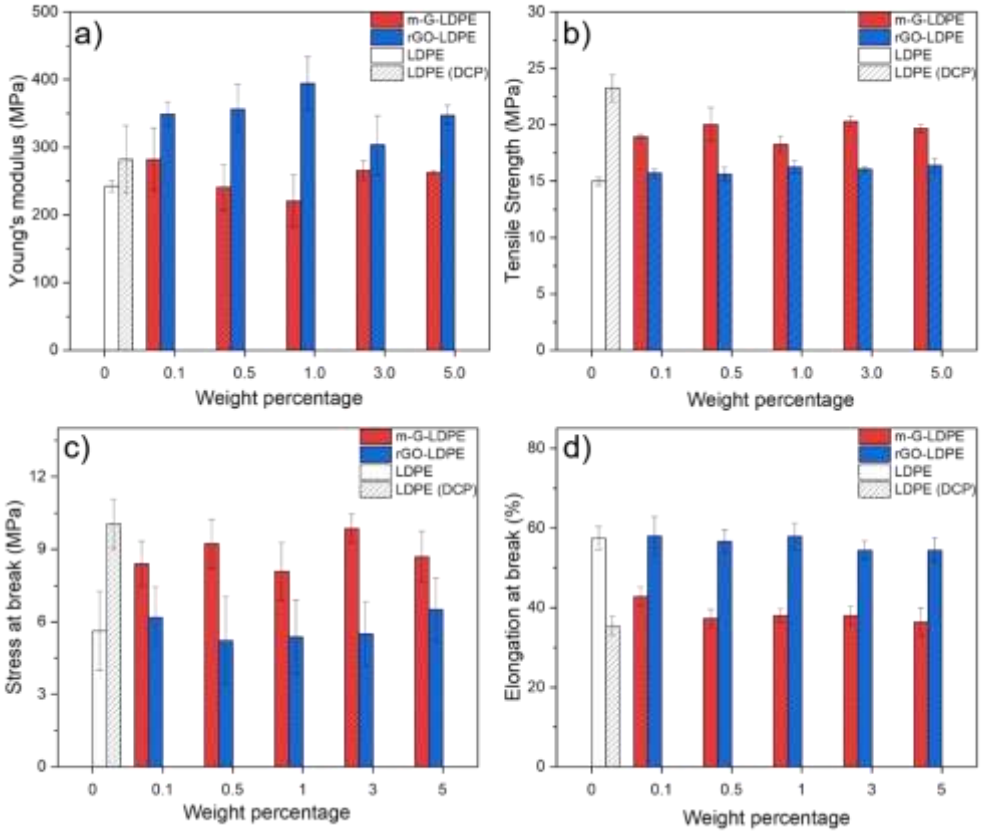

Figure 7. Variation in a) Young's modulus (E), b) tensile strength (σ), c) tensile stress at break (σ_b) and d) elongation at break (ε) of neat LDPE and composites of LDPE with 0.1 wt%, 0.5 wt%, 1.0 wt%, 3.0 wt% and 5.0 wt% rGO and m-G-LDPE composites.

The constrained LDPE chain mobility, a consequence of the crosslinking was studied using DMTA, specifically to probe the effect of rGO addition and crosslinking on the three molecular transitions (α, β, and γ) of LDPE. The γ transition occurs in the glass transition temperature range, typically between -110°C and -150°C, and is attributed to the crankshaft movement of methylene groups. The β transition occurs around -10°C and is associated with the relaxation of the side groups and chain segments present in the amorphous phase and the α phase occurs at 50°C which is attributed to the mobility of the chain segments in the crystalline phase [38, 49]. Figure S1 (Supplementary Information)

shows the tan δ_{max} (α-relaxation) peak for the composites at ~50°C, which decreases for the m-G-LDPE composites relative to neat LDPE. This is attributed to the decrease in the damping effect for the composites caused by the silane modified rGO making the material more elastic at higher temperatures [50]. Furthermore, the α peak position decreased with increasing rGO loading. As discussed above, the α region corresponds to the molecular motions in the crystalline phase and the insertion of modified rGO in to LDPE matrix hinders crystallite growth and results in higher crystal defects. At lower temperatures, the storage modulus also remained lower for the m-G-LDPE composites relative to neat LDPE, a result of the reduction in crystallinity for the composites, confirmed from the crystallinity values determined by DSC, see Table S2. However, the storage modulus gradually increases with increasing VTMOS-rGO loading in LDPE, particularly at 5 wt%. This is because the particle-particle motion is much stronger than that for the neat LDPE caused by the silane modification [51]. From Figure S1, the m-G-LDPE composites have higher tan δ values compared with neat LDPE in the glass transition temperature (T_g) range due to an increase in loss moduli. This increment in the damping behaviour can be attributed to the reduction in LDPE crystallinity caused by inclusion of the silane-modified graphene. This is further confirmed by the slight shift of T_g to lower temperatures for m-G-LDPE relative to the neat LDPE, see Table S1 [52]. Whereas, for the rGO-LDPE composites, the T_g shifted to lower temperatures initially for low rGO loading before increasing with further additions.

The extent of rGO dispersion and distribution in the LDPE matrix and the effect of crosslinking on the viscoelastic response of the polymer was studied using oscillatory rheology. The formation of a percolated rGO network will be manifest by a change in the elastic response of the polymer by displaying ‘pseudo’ solid-like properties which can be

detected by an increase in complex viscosity and storage modulus at low frequencies [53]. The change in storage modulus (G), loss modulus (G′) and complex viscosity (η*) for neat LDPE with and without DCP and, with increasing loadings of m-rGO (up to 5 wt%) as a function of frequency (ω) are shown in Figure 8. G′, G′′ and η* increased when the LDPE was cross-linked with DCP and/or when m-rGO was added, for G′, by about one order of magnitude, double that for G′′ confirming the greater increase in elastic than viscous response of the composite relative to neat LDPE [54]. Cross-linking of LDPE initiated by DCP results in some shear thinning behaviour and with addition of m-rGO, an increase in η* is also obtained, at lower ω. The transition from 'liquid-like' to more 'solid-like' behaviour at lower ω is indicative of the formation of an interconnected network within the matrix, which hinders polymer chain mobility. [55-56].

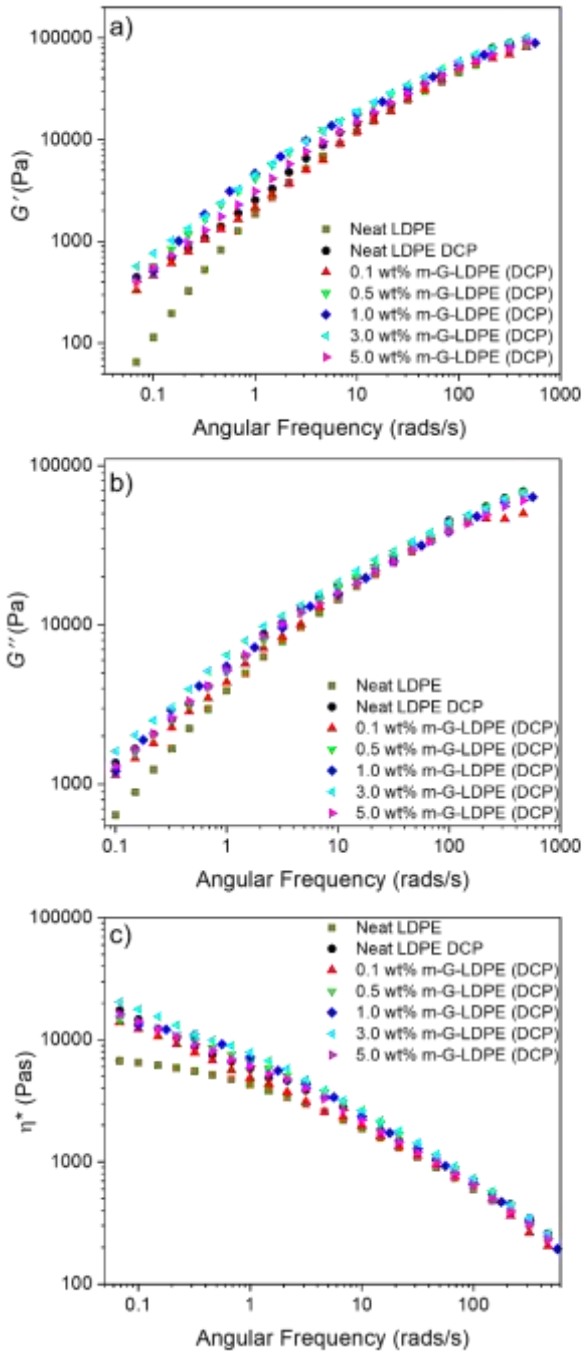

Figure 8. Variation in a): storage modulus (G), b): loss modulus (G″) and c) complex viscosity (η*) as a function of angular frequency (ω) for neat LDPE with and without 0.1 wt% DCP and the m-g-LDPE composites.

From the data shown in Figure 8 it is clear that crosslinking of LDPE with DCP alone or in the presence of silane modified rGO (m-g-LDPE) results in an increase in the elastic response of LDPE. This is proven when G′, G′′ and η* for blends of rGO and LDPE are compared with the same data for the m-g-LDPE composites, by way of example see Figure 9. For plots of G′ versus ω, when the rGO content is 0.1 wt%, G′ for m-G-LDPE was greater than that for rGO-LDPE but the same as for neat LDPE with DCP, therefore the increase in G′ can be attributed to cross-linking initiated by DCP rather than silane modification of rGO. However, as the loading of rGO was increased (up to 3 wt%), G′ of the composites with cross-linked silane modified rGO (i.e. m-g-LDPE) was higher than the corresponding blend of rGO and LDPE and, the neat LDPE with and without DCP, over much of the frequency range examined. Again, the cross-linked network

formed alters the elastic response of the polymer matrix [54].

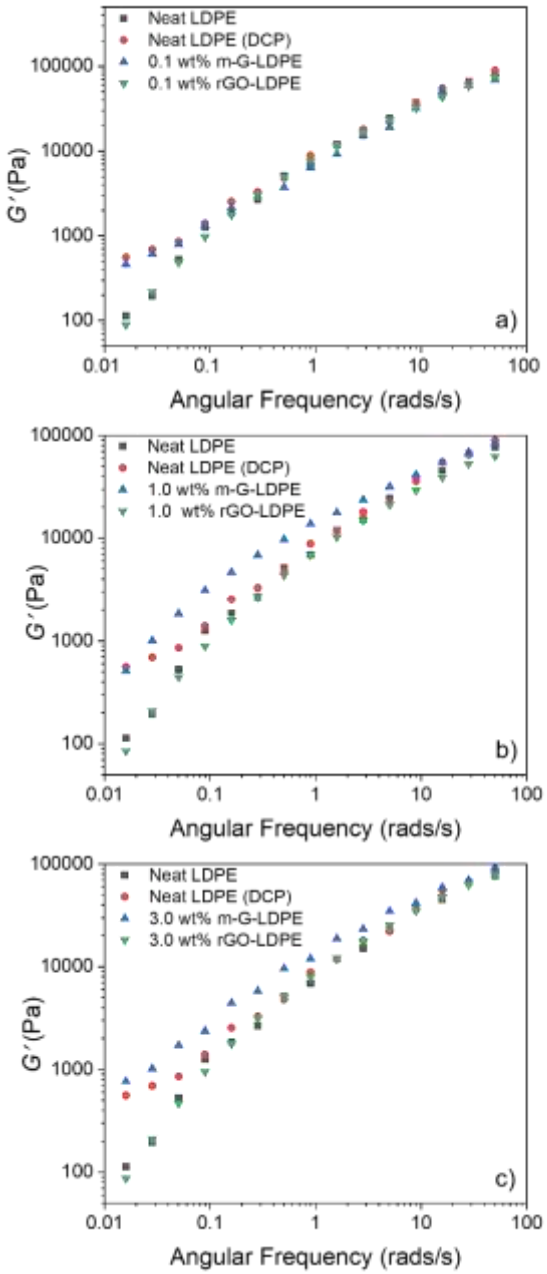

Figure 9. Variation in storage modulus (G′) as a function of angular frequency for neat LDPE, neat LDPE with DCP, blends of rGO and LDPE and, m-g-LDPE where the rGO loading is a) 0.1 wt%, b) 1.0 wt% and c) 3.0 wt%.

The transition from 'viscous-like' to more 'elastic-like' behaviour can be more accurately detected from the intersection or cross-over point of plots of G′and G′′versus ω, Figure 10**.** For neat LDPE, the cross-over point is at a high frequency, ω=31.6 rads/s, displaying viscous-like behaviour (G′>G) at the terminal region followed by a viscoelastic response at higher ω [57]. When a cross-linked silane functionalised rGO network is formed (i.e. m-g-LDPE composites), the frequency (ω) at which there was a crossover of the G′and G′′curves decreased relative to the blends of rGO and LDPE. The transition to more 'solid-like' behaviour caused by the formation of a crosslinked network also delays polymer chain relaxation (λ) which can be estimated using Equation 1, the values of ω and λ are listed in Table 1 [57];

$$\lambda . \omega = 1 \qquad (1)$$

where, ω is the cross-over frequency and λ is the relaxation time in seconds.

The cross-over frequency decreased from 31.62 rads/s for neat LDPE to 3.16 rads/s for the 0.5wt% m-g-LDPE, whereas for the corresponding un-crosslinked blend of rGO (0.5wt%) and LDPE it remained unchanged. The physical blending of rGO and LDPE did not alter the viscoelastic behaviour of LDPE in contrast to the effect of creating a crosslinked network of silane functionalised rGO and LDPE. This is even more evident for the 1.0 wt% m-g-LDPE composite as the cross-over frequency decreased further to 0.603 rads/s and the relaxation time is increased to 1.66 seconds. 1 wt% rGO was the optimum loading for the m-g-LDPE composites as it had the highest G′and G′′and lowest cross-over ω values, therefore displaying the most solid-like behaviour. Further increasing additions of rGO for the m-g-LDPE composites resulted in increased ω values up to 10 rad/s and shorter relaxation times down, to 0.10 seconds

Table 1. Crossover frequencies (ω) and relaxation times (λ) for blends of rGO-LDPE and cross-linked m-g-LDPE composites.

rGO Loading (wt%)	**ω (rads/s) rGO-LDPE**	**ω (rads/s) m-g-LDPE**	**λ (s) rGO-LDPE**	**λ (s) m-g-LDPE**
0.5	31.62	3.16	0.032	0.32
1.0	31.62	0.603	0.032	1.66
3.0	31.62	6.81	0.032	0.15
5.0	31.62	10	0.032	0.10

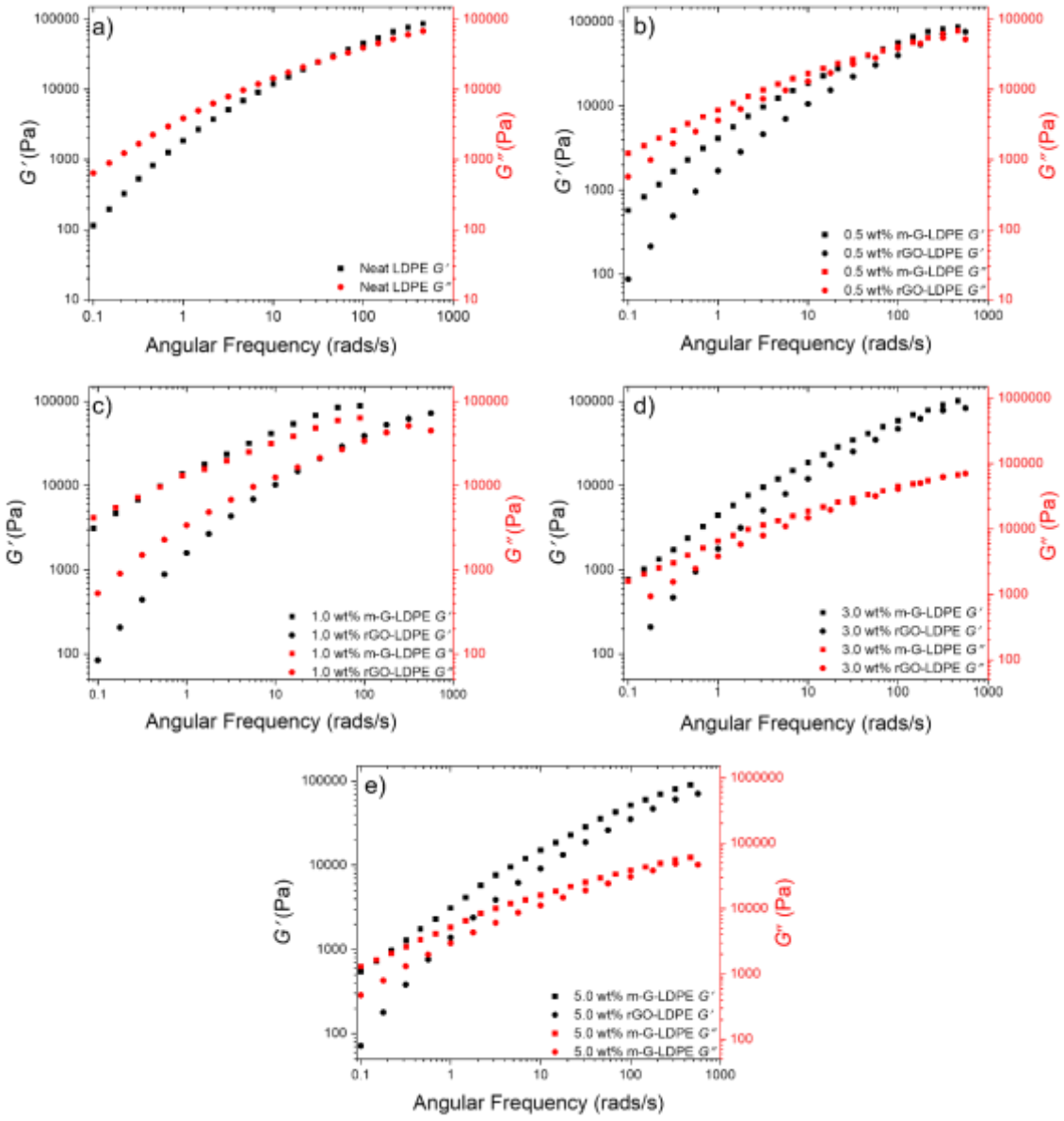

Figure 10. Plots of G′ and G′′ as a function of frequency (ω) for a) neat LDPE and comparing the physical blends of rGO and LDPE with the m-g-LDPE composites when the rGO loading is b) 0.5 wt%, c) 1.0 wt%, d) 3.0 wt% and e) 5.0 wt%.

The inclusion of rGO and the formation of a cross-linked silane modified rGO network in the LDPE matrix altered the crystallisation behaviour of LDPE. As listed in Table S2, the LDPE crystalline content decreased from 40% to 36% on reaction of LDPE

with DCP, cross-linking induced by the DCP initiator resulting in the formation of irregular structures within the chains that cannot be incorporated into the crystal lattice restricting polymer chain mobility and ultimately resulting in lower crystalline content [45]. For the rGO-LDPE composites, the addition of rGO results in increased crystalline content due to heterogeneous nucleation of LDPE by rGO [58]. However, the m-G-LDPE composites still have a slightly higher crystallinity than neat LDPE with DCP, as addition of DCP to neat LDPE initiates cross-linking between LDPE chains and therefore, reduced crystallinity. Inclusion of the DCP initiator in m-G-LDPE, also results in cross-linking via the pendant vinyl group of the silane modified rGO to the LDPE chains. The m-G-LDPE is less crystalline that neat LDPE, as the crystallisation of LDPE is hindered by the presence of cross-links and stacks of poorly exfoliated rGO [59].

The XRD pattern of LDPE is typical of the orthorhombic crystal structure having two main peaks at $2\theta = \sim 25°$ and $\sim 27°$ corresponding to (110) and (200) basal planes, respectively, see Figure 11 [40]. There is a slight shoulder to the left of this peak observed at $2\theta = \sim 22°$ which can be attributed to the diffraction peak for the monoclinic $(\bar{1}10)$ crystal structure of PE [60]. The composites had similar diffraction patterns, irrespective if they were simple blends of rGO and LDPE or the cross-linked LDPE composite systems. The broad and low intense diffraction peak between 6 and 12 2θ became more intense the greater the rGO loading, behaviour attributed to the exfoliation of rGO when modified with VTMOS within the polymer matrix [59]. The intensity of the peaks associated with the (110) and (200) basal planes for neat LDPE and, the blends of rGO and LDPE are similar. However, for the cross-linked m-G-LDPE these peaks are more intense suggesting smaller more perfectly packed PE crystallites. While the LDPE is crosslinked to both the silane networks formed interstitially between expanded rGO layers and itself,

there remains a significant amount of LDPE free to crystallise. The majority of crosslinking must take place between stacks of silane functionalised rGO and LDPE and between LDPE chains close to these stacks to give the structure seen in Figure 4.

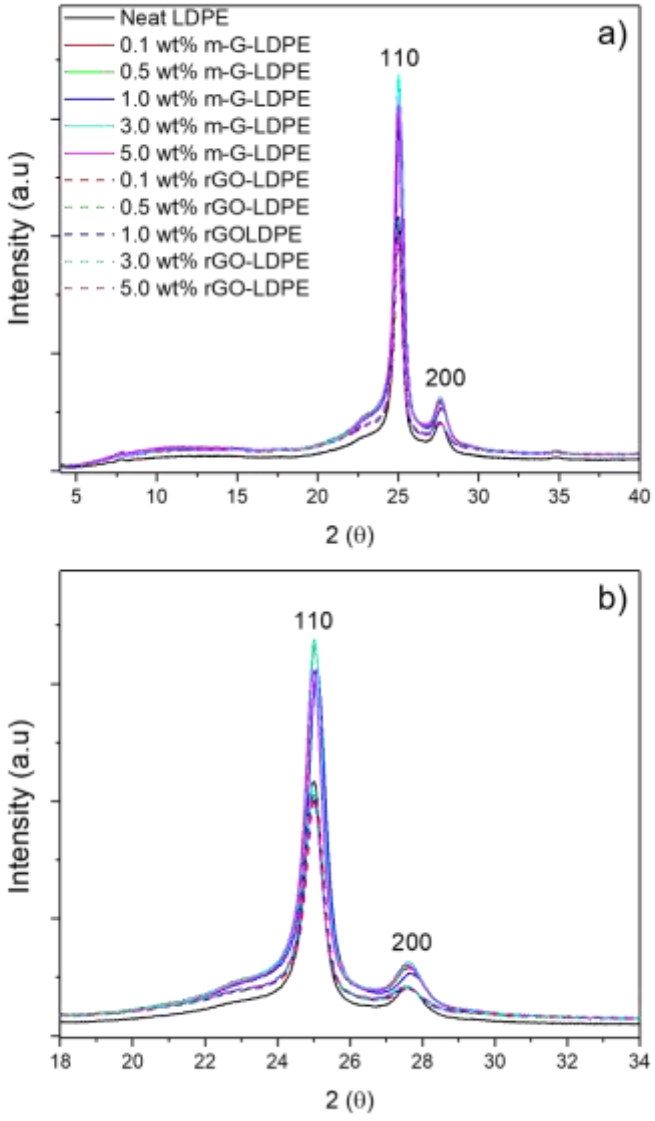

Figure 11. a) XRD patterns for neat LDPE, blends of rGO and LDPE and m-G-LDPE and, b) expanded view of a) in the 18 to 34 2θ range.

The inclusion of rGO and formation of crosslinks altered the thermal stability of LDPE. Figure S2 shows the TGA and the DTG profiles for blends of rGO and LDPE and the m-G-LDPE composites. The temperature for the onset of degradation and for 10% weight loss ($T_{10\%}$) is listed in Table ST3. For neat LDPE the onset started at 390 °C but the polymer had completely decomposed by 490°C. The temperature at 10% weight loss ($T_{10\%}$) occurred was 423°C and from the corresponding DTG curve (Figure S2b)), degradation was a single process, known to be due to thermal scission of C-C bonds [55]. A single degradation process was also obtained for the rGO-LDPE blends and m-G-LDPE composites, however for the latter the onset of thermal degradation was delayed with increasing silane modified rGO loading, up to 18°C for 5.0 wt%. For the same filler content, the $T_{10\%}$ value for rGO-LDPE was 21°C lower than that for m-G-LDPE. This enhancement in thermal stability for m-G-LDPE is associated with the thermal degradation of the crosslinks requiring a higher activation energy that the physical blend of rGO and LDPE [61]. Moreover, the 3D silane network is bonded to rGO forming a cross-linked 'sandwich' like structure, again delaying the onset of thermal degradation [55]. During heating, the Si-O-Si bonds form thermally stable silica compounds which migrate to the char surface forming a protective layer and retarding the degradation of the polymer matrix at higher temperatures [62].

4. Conclusions

VTMOS functionalised rGO was mixed with LDPE and DCP free radical initiator in an extruder to produce a cross-linked network of VTMOS-rGO-LDPE (m-G-LDPE). ^{13}C MAS NMR experiments confirmed the reaction of the pendant vinyl group on the silane with the LDPE chains *via* a free radical initiation step. An additional resonance at 26 ppm obtained is from the methyl attachment from the vinyl group to the LDPE chains.

The single resonance peak at 28 ppm for LDPE split into three peaks due to the cross-linking of small polymer branches to the main longer branches, confirming inter- and intra-LDPE chain cross-linking. Functionalisation of rGO was also confirmed by Raman spectroscopy. SEM and TEM imaging and elemental mapping showed the silane network forms spherical particles located between rGO layers.

The resultant cross-linked m-G-LDPE composites had tensile strengths (σ) some 31% greater than neat LDPE and 9% greater than the corresponding physical blends of rGO and LDPE. The corresponding figures for tensile stress at break (σ_b) were 55% and 16%, respectively. The inclusion of a cross-linked network enhanced the tensile strength of LDPE. As expected, there was a decrease in the elongation at break (ε) (related to ductility) for the m-G-LDPE composites. Interestingly, the physical blends of rGO and LDPE were more stiff (↑E values) than the cross-linked m-G-LDPE composites. This suggests the degree of cross-linking is not extensive per unit volume of matrix, but perhaps predominately within the rGO stacks and between these stacks and neighbouring LDPE chains. The inclusion of cross-linking resulted in ~10% reduction in LDPE crystalline content and better packing of LDPE crystallites.

The storage modulus (G') of the m-G-LDPE composites, was greater than that measured for LDPE alone, the cross-linked structure increased the elastic response of LDPE at lower frequencies. Shear thinning behaviour was observed for the m-G-LDPE composites, mainly due to cross-linking however, silane modification further enhanced complex viscosity (η^*) at lower frequencies. The formation of a 3D interconnected silane functionalised rGO and LDPE network hinders macromolecular chain mobility inducing a transition from 'liquid-like' to 'solid-like' behaviour. The storage (G') and loss moduli (G″) of m-G-LDPE were greater than that for the physical blends of rGO and LDPE.

Moreover, the cross-over point at which G′and G′′intersected, by way of example, for m-G-LDPE with 1 wt% rGO reached a cross-over point at 0.603 rads/s compared with 31.62 rads/s for neat LDPE and no change for the physical blends of rGO and LDPE. Silane modification of rGO and inclusion in LDPE via crosslinking resulted in the crossover point attained at lower frequencies and therefore the m-G-LDPE composites displayed the most solid-like behaviour.

From TGA the onset of thermal degradation of LDPE was delayed by up to 18 °C when cross-linked with VTMOS-rGO for a 5 wt% rGO loading. Similar behaviour was observed for the $T_{10\%}$ value which was 21°C higher for the m-G-LDPE composites relative to physical blends of rGO and LDPE and 30 °C higher when compared with neat LDPE. The 3D silane functionalised rGO network cross-linked to LDPE formed 'sandwich-like' structures within the LDPE matrix, combined with inter- and intra-LDPE cross-linking required a higher activation energy for thermal degradation.

Associated Content

Supporting Information

Dynamic mechanical thermal analysis of LDPE, LDPE-DCP and m-G-LDPE (S1), TGA and derivative curves for LDPE, rGO-LDPE and m-g-LDPE (S2), Glass transition temperature tabulated for of LDPE, LDPE-DCP, rGO-LDPE and m-G-LDPE composites (Table S1), Melting temperature, crystallization temperature, enthalpy of melting and heating and crystallinity values tabulated for LDPE, LDPE-DCP, rGO-LDPE and m-G-LDPE composites (Table S2), thermal degradation temperature and maximum decomposition temperature tabulated for LDPE, LDPE-DCP, rGO-LDPE and m-G-LDPE composites (Table S3).

Acknowledgements

SA thanks EPSRC and Jaguar Land Rover for funding an iCASE PhD studentship. JVH acknowledges support for the solid state NMR instrumentation at Warwick used in this research which was funded by EPSRC (grant numbers EP/M028186/1 & EP/K024418/1) and the University of Warwick, with additional partial funding being provided through the Birmingham Science City Advanced Materials Projects 1 and 2, which were supported by Advantage West Midlands (AWM) and the European Regional Development Fund (ERDF).

References

1. Hu, H.; Chen, G., Electrochemically modified graphite nanosheets and their nanocomposite films with poly(vinyl alcohol). *Polym. Compos.* **2010,** *31* (10), 1770-1775.

2. Compton, O. C.; Jain, B.; Dikin, D. A.; Abouimrane, A.; Amine, K.; Nguyen, S. T., Chemically Active Reduced Graphene Oxide with Tunable C/O Ratios. *ACS Nano* **2011,** *5* (6), 4380-4391.

3. Zhang, J.; Xu, Y.; Cui, L.; Fu, A.; Yang, W.; Barrow, C.; Liu, J., Mechanical properties of graphene films enhanced by homo-telechelic functionalized polymer fillers via π–π stacking interactions. *Composites Part A* **2015,** *71*, 1-8.

4. Chen, H.; Müller, M. B.; Gilmore, K. J.; Wallace, G. G.; Li, D., Mechanically Strong, Electrically Conductive, and Biocompatible Graphene Paper. *Adv. Mater.* **2008,** *20* (18), 3557-3561.

5. Lee, C.; Wei, X.; Kysar, J. W.; Hone, J., Measurement of the Elastic Properties and Intrinsic Strength of Monolayer Graphene. *Science* **2008,** *321* (5887), 385-388.

6. Rohini, R.; Katti, P.; Bose, S., Tailoring the interface in graphene/thermoset polymer composites: A critical review. *Polymer* **2015,** *70*, A17-A34.

7. Liao, L.; Peng, H.; Liu, Z., Chemistry Makes Graphene beyond Graphene. *JACS* **2014,** *136* (35), 12194-12200.

8. Ferreira, F. V.; Cividanes, L.; Brito, F. S.; de Menezes, B. R. C.; Franceschi, W.; Simonetti, E. A. N.; Thim, G. P., *Functionalizing Graphene and Carbon Nanotubes: A Review*. Springer International Publishing: 2016.

9. Geim, A. K.; Novoselov, K. S., The rise of graphene. *Nat Mater* **2007,** *6* (3), 183-191.

10. Foster, C.; P. Down, M.; Zhang, Y.; Ji, X.; Rowley-Neale, S.; Smith, G.; J. Kelly, P.; Banks, C., *3D Printed Graphene Based Energy Storage Devices*. 2017; Vol. 7, p 42233.

11. Yang, K.; Zhang, S.; Zhang, G.; Sun, X.; Lee, S.-T.; Liu, Z., Graphene in Mice: Ultrahigh In Vivo Tumor Uptake and Efficient Photothermal Therapy. *Nano Lett* **2010,** *10* (9), 3318-3323.

12. Sun, X.; Liu, Z.; Welsher, K.; Robinson, J. T.; Goodwin, A.; Zaric, S.; Dai, H., Nano-Graphene Oxide for Cellular Imaging and Drug Delivery. *Nano Res.* **2008,** *1* (3), 203-212.

13. Potts, J. R.; Dreyer, D. R.; Bielawski, C. W.; Ruoff, R. S., Graphene-based polymer nanocomposites. *Polymer* **2011,** *52* (1), 5-25.

14. Guan, L.-Z.; Wan, Y.-J.; Gong, L.-X.; Yan, D.; Tang, L.-C.; Wu, L.-B.; Jiang, J.-X.; Lai, G.-Q., Toward effective and tunable interphases in graphene oxide/epoxy composites by grafting different chain lengths of polyetheramine onto graphene oxide. *Journal of Materials Chemistry A* **2014,** *2* (36), 15058-15069.

15. Barber, A. H.; Cohen, S. R.; Wagner, H. D., Measurement of carbon nanotube–polymer interfacial strength. *Appl. Phys. Lett.* **2003,** *82* (23), 4140-4142.

16. Kasaliwal, G. R.; Villmow, T.; Pegel, S.; Pötschke, P., 4 - Influence of material and processing parameters on carbon nanotube dispersion in polymer melts. In *Polymer–Carbon Nanotube Composites*, Woodhead Publishing: 2011; pp 92-132.

17. Wei, P.; Bai, S., Fabrication of a high-density polyethylene/graphene composite with high exfoliation and high mechanical performance via solid-state shear milling. *RSC Adv.* **2015,** *5* (114), 93697-93705.

18. Konios, D.; Stylianakis, M. M.; Stratakis, E.; Kymakis, E., Dispersion behaviour of graphene oxide and reduced graphene oxide. *J. Colloid Interface Sci.* **2014,** *430*, 108-112.

19. Thomas, H. R.; Day, S. P.; Woodruff, W. E.; Vallés, C.; Young, R. J.; Kinloch, I. A.; Morley, G. W.; Hanna, J. V.; Wilson, N. R.; Rourke, J. P., Deoxygenation of Graphene Oxide: Reduction or Cleaning? *Chem. Mater.* **2013,** *25* (18), 3580-3588.

20. Antonucci, J. M.; Dickens, S. H.; Fowler, B. O.; Xu, H. H. K.; McDonough, W. G., Chemistry of Silanes: Interfaces in Dental Polymers and Composites. *Journal of Research of the National Institute of Standards and Technology* **2005,** *110* (5), 541-558.

21. Ahmadi, A.; Ramezanzadeh, B.; Mahdavian, M., Hybrid silane coating reinforced with silanized graphene oxide nanosheets with improved corrosion protective performance. *RSC Adv.* **2016,** *6* (59), 54102-54112.

22. Haeri, S. Z.; Asghari, M.; Ramezanzadeh, B., Enhancement of the mechanical properties of an epoxy composite through inclusion of graphene oxide nanosheets functionalized with silica nanoparticles through one and two steps sol-gel routes. *Prog. Org. Coat.* **2017,** *111*, 1-12.

23. Xu, P.; Yan, X.; Cong, P.; Zhu, X.; Li, D., Silane coupling agent grafted graphene oxide and its modification on polybenzoxazine resin. *Compos. Interfaces* **2017,** *24* (7), 635-648.

24. Lee, C. Y.; Bae, J.-H.; Kim, T.-Y.; Chang, S.-H.; Kim, S. Y., Using silane-functionalized graphene oxides for enhancing the interfacial bonding strength of carbon/epoxy composites. *Composites Part A* **2015,** *75*, 11-17.

25. Pourhashem, S.; Rashidi, A.; Vaezi, M. R.; Bagherzadeh, M. R., Excellent corrosion protection performance of epoxy composite coatings filled with amino-silane functionalized graphene oxide. *Surf. Coat. Technol.* **2017,** *317*, 1-9.

26. Wang, X.; Xing, W.; Zhang, P.; Song, L.; Yang, H.; Hu, Y., Covalent functionalization of graphene with organosilane and its use as a reinforcement in epoxy composites. *Compos. Sci. Technol.* **2012,** *72* (6), 737-743.

27. Lee, C. Y.; Le, Q. V.; Kim, C.; Kim, S. Y., Use of silane-functionalized graphene oxide in organic photovoltaic cells and organic light-emitting diodes. *PCCP* **2015,** *17* (14), 9369-9374.

28. Wan, Y.-J.; Gong, L.-X.; Tang, L.-C.; Wu, L.-B.; Jiang, J.-X., Mechanical properties of epoxy composites filled with silane-functionalized graphene oxide. *Composites Part A* **2014,** *64*, 79-89.

29. Pourhashem, S.; Vaezi, M. R.; Rashidi, A.; Bagherzadeh, M. R., Distinctive roles of silane coupling agents on the corrosion inhibition performance of graphene oxide in epoxy coatings. *Prog. Org. Coat.* **2017,** *111*, 47-56.

30. Ramezanzadeh, B.; Haeri, Z.; Ramezanzadeh, M., A facile route of making silica nanoparticles-covered graphene oxide nanohybrids (SiO2-GO); fabrication of SiO2-GO/epoxy composite coating with superior barrier and corrosion protection performance. *Chem. Eng. J.* **2016,** *303*, 511-528.

31. Haeri, S. Z.; Ramezanzadeh, B.; Asghari, M., A novel fabrication of a high performance SiO2-graphene oxide (GO) nanohybrids: Characterization of thermal properties of epoxy nanocomposites filled with SiO2-GO nanohybrids. *J. Colloid Interface Sci.* **2017,** *493*, 111-122.

32. Pourhashem, S.; Vaezi, M. R.; Rashidi, A., Investigating the effect of SiO2-graphene oxide hybrid as inorganic nanofiller on corrosion protection properties of epoxy coatings. *Surface & Coatings Technology* **2017,** *311*, 282-294.

33. A. A. Yussuf, E. K., L. Alban, Silane grafting and crosslinking of metallocene-catalysed LLDPE and LDPE. *Malaysian polymer journal* **2007,** *2* (2), 58-71.

34. Zhang, H.-B.; Zheng, W.-G.; Yan, Q.; Yang, Y.; Wang, J.-W.; Lu, Z.-H.; Ji, G.-Y.; Yu, Z.-Z., Electrically conductive polyethylene terephthalate/graphene nanocomposites prepared by melt compounding. *Polymer* **2010,** *51* (5), 1191-1196.

35. Lin, S.; Anwer, M. A. S.; Zhou, Y.; Sinha, A.; Carson, L.; Naguib, H. E., Evaluation of the thermal, mechanical and dynamic mechanical characteristics of modified graphite nanoplatelets and graphene oxide high-density polyethylene composites. *Composites Part B* **2018,** *132*, 61-68.

36. Abbas, S. S.; Rees, G. J.; Kelly, N. L.; Dancer, C. E. J.; Hanna, J. V.; McNally, T., Facile silane functionalization of graphene oxide. *Nanoscale* **2018,** *10* (34), 16231-16242.

37. Shah, G. B.; Fuzail, M.; Anwar, J., Aspects of the crosslinking of polyethylene with vinyl silane. *J. Appl. Polym. Sci.* **2004,** *92* (6), 3796-3803.

38. Zhou, Y.; Fan, M., Recycled tyre rubber-thermoplastic composites through interface optimisation. *RSC Adv.* **2017,** *7* (47), 29263-29270.

39. Bugada, D. C.; Rudin, A., Branching in low density polyethylene by 13C-NMR. *Eur. Polym. J.* **1987,** *23* (10), 809-818.

40. Lei, H.; Liu, Z.; He, C.; Zhang, S.-C.; Liu, Y.-Q.; Hua, C.-J.; Li, X.-M.; Li, F.; Chen, C.-M.; Cai, R., Graphene enhanced low-density polyethylene by pretreatment and melt compounding. *RSC Adv.* **2016,** *6* (103), 101492-101500.

41. Strobl, G. R.; Hagedorn, W., Raman spectroscopic method for determining the crystallinity of polyethylene. *Journal of Polymer Science: Polymer Physics Edition* **1978,** *16* (7), 1181-1193.

42. Peterlin, A., Molecular model of drawing polyethylene and polypropylene. *J. Mater. Sci.* **1971,** *6* (6), 490-508.

43. Kolanthai, E.; Bose, S.; Bhagyashree, K. S.; Bhat, S. V.; Asokan, K.; Kanjilal, D.; Chatterjee, K., Graphene scavenges free radicals to synergistically enhance structural properties in a gamma-irradiated polyethylene composite through enhanced interfacial interactions. *PCCP* **2015,** *17* (35), 22900-22910.

44. Gu, J.; Xu, H.; Wu, C., The Effect of PP and Peroxide on the Properties and Morphology of HDPE and HDPE/PP Blends. *Adv. Polym. Tech.* **2013,** *32* (1), 21326.

45. Nilsson, S.; Hjertberg, T.; Smedberg, A., Structural effects on thermal properties and morphology in XLPE. *Eur. Polym. J.* **2010,** *46* (8), 1759-1769.

46. Ma, W.-S.; Li, J.; Zhao, X.-S., Improving the thermal and mechanical properties of silicone polymer by incorporating functionalized graphene oxide. *J. Mater. Sci.* **2013,** *48* (15), 5287-5294.

47. Araújo, R. S.; Oliveira, R. J. B.; Libório, P.; de Fátima V. Marques, M., Influence of Carbon Nanoparticles on Thermal, Mechanical and Rheological Properties

of Polypropylene Nanocomposites Modified with Vinyl Trimethoxysilane. *Macromolecular Symposia* **2016,** *368* (1), 107-115.

48. Liu, S.-Q.; Gong, W.-G.; Zheng, B.-C., The Effect of Peroxide Cross-Linking on the Properties of Low-Density Polyethylene. *Journal of Macromolecular Science, Part B* **2014,** *53* (1), 67-77.

49. Fim, F. d. C.; Basso, N. R. S.; Graebin, A. P.; Azambuja, D. S.; Galland, G. B., Thermal, electrical, and mechanical properties of polyethylene–graphene nanocomposites obtained by in situ polymerization. *J. Appl. Polym. Sci.* **2013,** *128* (5), 2630-2637.

50. Kuila, T.; Bose, S.; Mishra, A. K.; Khanra, P.; Kim, N. H.; Lee, J. H., Effect of functionalized graphene on the physical properties of linear low density polyethylene nanocomposites. *Polymer. Test.* **2012,** *31* (1), 31-38.

51. Huang, Y.; Jiang, S.; Wu, L.; Hua, Y., Characterization of LLDPE/nano-SiO2 composites by solid-state dynamic mechanical spectroscopy. *Polymer. Test.* **2004,** *23* (1), 9-15.

52. Khonakdar, H. A.; Wagenknecht, U.; Jafari, S. H.; Hässler, R.; Eslami, H., Dynamic mechanical properties and morphology of polyethylene/ethylene vinyl acetate copolymer blends. *Adv. Polym. Tech.* **2004,** *23* (4), 307-315.

53. Goswami, J.; Davis, V. A., Viscoelasticity of Single-Walled Carbon Nanotubes in Unsaturated Polyester Resin: Effects of Purity and Chirality Distribution. *Macromol.* **2015,** *48* (23), 8641-8650.

54. Mun, S. C.; Kim, M.; Prakashan, K.; Jung, H. J.; Son, Y.; Park, O. O., A new approach to determine rheological percolation of carbon nanotubes in microstructured polymer matrices. *Carbon* **2014,** *67*, 64-71.

55. El Achaby, M.; Qaiss, A., Processing and properties of polyethylene reinforced by graphene nanosheets and carbon nanotubes. *Materials & Design* **2013,** *44*, 81-89.

56. Krishnamoorti, R.; Giannelis, E. P., Rheology of End-Tethered Polymer Layered Silicate Nanocomposites. *Macromol.* **1997,** *30* (14), 4097-4102.

57. Tripathi, S. N.; Malik, R. S.; Choudhary, V., Melt rheology and thermomechanical behavior of poly(methyl methacrylate)/reduced graphene oxide nanocomposites. *Polym. Adv. Technol.* **2015,** *26* (12), 1558-1566.

58. El Achaby, M.; Arrakhiz, F.-E.; Vaudreuil, S.; el Kacem Qaiss, A.; Bousmina, M.; Fassi-Fehri, O., Mechanical, thermal, and rheological properties of graphene-based polypropylene nanocomposites prepared by melt mixing. *Polym. Compos.* **2012,** *33* (5), 733-744.

59. Cruz-Aguilar, A.; Navarro-Rodríguez, D.; Pérez-Camacho, O.; Fernández-Tavizón, S.; Gallardo-Vega, C. A.; García-Zamora, M.; Barriga-Castro, E. D., High-density polyethylene/graphene oxide nanocomposites prepared via in situ

polymerization: Morphology, thermal, and electrical properties. *Materials Today Communications* **2018,** *16*, 232-241.

60. Olmos, D.; Rodríguez-Gutiérrez, E.; González-Benito, J., Polymer structure and morphology of low density polyethylene filled with silica nanoparticles. *Polym. Compos.* **2012,** *33* (11), 2009-2021.

61. Marosfői, B. B.; Szabó, A.; Marosi, G.; Tabuani, D.; Camino, G.; Pagliari, S., Thermaland spectroscopic characterization of polypropylene-carbon nanotube composites. *J. Therm. Anal. Calorim.* **2006,** *86* (3), 669-673.

62. Chiang, C. L.; Yang, J. M., 11 - Flame retardance and thermal stability of polymer/graphene nanosheet oxide composites. In *Novel Fire Retardant Polymers and Composite Materials*, Wang, D.-Y., Ed. Woodhead Publishing: 2017; pp 295-312.